Design optimization of a high-speed twin-stage compressor for next-gen aircraft environmental control system

Giuffre, Andrea; Colonna, Piero; Pini, Matteo

DOI
10.1115/GT2022-81690

Publication date
2022

Document Version
Final published version

Published in
Turbomachinery - Design Methods and CFD Modeling for Turbomachinery; Ducts, Noise, and Component Interactions

Citation (APA)
Giuffre, A., Colonna, P., & Pini, M. (2022). Design optimization of a high-speed twin-stage compressor for next-gen aircraft environmental control system. In *Turbomachinery - Design Methods and CFD Modeling for Turbomachinery; Ducts, Noise, and Component Interactions* Article V10CT32A019 (Proceedings of the ASME Turbo Expo; Vol. 10-C). American Society of Mechanical Engineers (ASME). https://doi.org/10.1115/GT2022-81690

Proceedings of ASME Turbo Expo 2022
Turbomachinery Technical Conference and Exposition
GT2022
June 13-17, 2022, Rotterdam, The Netherlands

GT2022-81690

DESIGN OPTIMIZATION OF A HIGH-SPEED TWIN-STAGE COMPRESSOR FOR NEXT-GEN AIRCRAFT ENVIRONMENTAL CONTROL SYSTEM

Andrea Giuffre'
Propulsion and Power
Faculty of Aerospace Engineering
Delft University of Technology
Delft, The Netherlands, 2629HS

Piero Colonna
Propulsion and Power
Faculty of Aerospace Engineering
Delft University of Technology
Delft, The Netherlands, 2629HS

Matteo Pini*
Propulsion and Power
Faculty of Aerospace Engineering
Delft University of Technology
Delft, The Netherlands, 2629HS

ABSTRACT

The environmental control system (ECS) is the largest auxiliary power consumer, i.e, around 75% of non-propulsive power, among the aircraft subsystems. The adoption of a novel ECS architecture, based on an electrically-driven vapor compression cycle system, can enable a twofold increase of coefficient of performance (COP), as compared to the conventional air cycle machine (ACM). The core of this technology is a high-speed, miniature centrifugal compressor, consisting of two impellers mounted in back-to-back configuration, and running on gas bearings operating with refrigerant. The fluid dynamic design optimization of the twin-stage compressor, to be installed in the vapor compression cycle test rig under realization at Delft University of Technology, is documented in this paper. First, the scaling analysis for centrifugal compressor is extended to provide guidelines for the design of twin-stage machines. Then, a multi-objective conceptual design optimization is performed by resorting to an in-house reduced-order model (ROM), coupled to a genetic algorithm. The fluid dynamic performance and the structural integrity of the optimal design are assessed by means of a hybrid framework, encompassing CFD and ROMs, and by FEA. The results show that it is possible to design a twin-stage compressor for the target application, featuring an average efficiency higher than 70%, a maximum compression ratio exceeding 9, and an operating range of 0.27 *at the design rotational speed, despite the detrimental effects of motor cooling and miniature size.*

NOMENCLATURE

Symbols

E	Young modulus
D	Diameter
F_{ax}	Axial thrust
H	Blade height
h	Specific enthalpy
k	Impeller shape factor
L_{ax}	Axial length
Ma	Mach number
$\dot{m}$	Mass flow rate
N_{bl}	Number of blades
N_{split}	Number of splitter blades
OR	Operating range
P	Pressure
$\dot{Q}$	Heat flow rate
R	Radius
Ra	Surface roughness
Re	Reynolds number
t	Thickness
T	Temperature - torque
T_{m}	Melting point temperature
$\dot{V}$	Volumetric flow rate
U	Peripheral speed
$\dot{V}$	Volumetric flow rate
V	Absolute velocity
W	Power - relative velocity
$\boldsymbol{x}$	Design variables

---

*m.pini@tudelft.nl

α	Absolute flow angle
β	Compression ratio
γ_{Pv}	Isentropic pressure-volume exponent
ε_{b}	Back face clearance
ε_{t}	Tip clearance gap
η	Efficiency
κ_{s}	Compression ratio splitting factor
ν	Poisson's ratio
ϕ_{t1}	Swallowing capacity
ψ	Work coefficient
ρ	Density
$\boldsymbol{\sigma}$	Stage dimensionless geometrical characteristics
σ_{y}	Yielding stress
σ_{uts}	Ultimate tensile strength
Ω	Rotational speed

Subscripts

b	Bearings
bl	Blade
des	Design point
el	Electric
h	Hub
hd	Hydraulic
is	Isentropic
le	Leading edge
r	Ratio
s	Shroud
s1	First stage
s2	Second stage
t	Total
te	Trailing edge
ts	Total-to-static
tt	Total-to-total

Abbreviations

ACM	Air cycle machine
ECS	Environmental control system
IRIS	Inverse Rankine integrated system
ROM	Reduced-order model
VCC	Vapor compression cycle

INTRODUCTION

The aviation industry is under increasing pressure to improve aircraft fuel efficiency for economic, environmental and societal reasons. Fuel efficiency[1] has roughly doubled since 1960, albeit at a diminishing rate [1]. The improvements can be mostly attributed to the replacement of traditional turbojets engines with modern high-bypass ratio turbofans. On the opposite, the contribution of aircraft subsystems to fuel efficiency enhancements has been negligible [2]. The environmental control system (ECS) is the largest consumer of non-propulsive power among the aircraft subsystems, accounting for up to 3-5% of the total energy consumption [3]. However, technological innovations in the ECS architectures have been limited since the 1960s, with few exceptions, e.g. the electrically-powered ECS mounted on the Boeing 787. Conventional pneumatic systems extract from the engines more power than is needed in most operating conditions, causing excess energy to be dumped overboard. The use of electrical power is more efficient than engine-generated pneumatic power, leading to a predicted improvement in fuel consumption in the range of 1-2% at cruise conditions [4]. Furthermore, the adoption of an electrically-powered ECS enables a reduction of maintenance costs and an overall increase of system reliability, due to the removal of the maintenance-intensive bleed system.

In addition to the advantages related to ECS electrification, a further reduction of fuel consumption can be arguably achieved by replacing the bleedless air cycle machine (ACM), i.e. an inverse Brayton cycle, with a more efficient electrically-driven vapor compression cycle (VCC), leading to a potential twofold increase of coefficient of performance (COP). The technical feasibility and the performance of an electrically-powered VCC system for next-generation ECS will be investigated by means of a new experimental facility currently under realization at Delft university of Technology. At the core of the IRIS (Inverse Rankine Integrated System) test rig, there is a high-speed twin-stage centrifugal compressor running on foil bearings, lubricated by the refrigerant vapor. The reduced size, the absence of oil lubricant in the circuit, and the predicted superior performance over traditional scroll compressors make this technology very suitable for airborne applications.

OBJECTIVE

The feasibility of a miniature centrifugal compressor running on gas bearings for domestic heat pump applications has been demonstrated by Schiffmann et al. [5, 6]. The influence of size and working fluid on various design aspects concerning single-stage high-speed compressors has been systematically investigated in a recent work [7]. However, the design of a twin-stage compressor, featuring two compressor wheels mounted in back-to-back configuration on the same shaft, involves additional consideration regarding the split of the duty among the two stages, the balance of axial thrust produced by the two impellers, the cooling of the bearings, and that of the electric motor.

The objectives of this work are: i) the extension of the scaling analysis for twin-stage compressors to support the designer in the choice of the non-dimensional parameters characterizing the conceptual design of the two stages; ii) the multi-objective conceptual design optimization of the twin-stage compressor to be installed in the IRIS test rig; iii) the performance characteriza-

---

[1] Defined by the number of passengers times flight distance per unit fuel burn.

TABLE 1: Non-dimensional geometrical characteristics of a single-stage centrifugal compressor, collected in the vector $\boldsymbol{\sigma}$. The main geometrical features of the prescribed compressor configuration are displayed in Fig. 3.

Description	Definition
Impeller shape factor	$k = 1 - \left(\frac{R_{1,\mathrm{h}}}{R_{1,\mathrm{s}}}\right)^2$
Number of blades	$N_{\mathrm{bl}},\ N_{\mathrm{split}}$
Diffuser radius ratio	R_3/R_2
Diffuser blade height ratio	$H_{\mathrm{r,pinch}} = \frac{H_3 - H_2}{H_2(R_2/R_{\mathrm{pinch}} - 1)}$
Diffuser pinch radius ratio	$R_{\mathrm{r,pinch}} = \frac{R_{\mathrm{pinch}} - R_2}{R_3 - R_2}$
Non-dimensional length	L_{ax}/R_2
Leading edge thickness ratio	$\frac{t_{\mathrm{le}}(N_{\mathrm{bl}} + N_{\mathrm{split}})}{2\pi R_1}$
Trailing edge thickness ratio	$\frac{t_{\mathrm{te}}(N_{\mathrm{bl}} + N_{\mathrm{split}})}{2\pi R_1}$
Relative tip clearance	$\varepsilon_{\mathrm{t}}/H_2$
Relative back face clearance	$\varepsilon_{\mathrm{b}}/H_2$
Relative surface roughness	$Ra/D_{\mathrm{hd,imp}}$
Shaft radius ratio	$R_{\mathrm{shaft}}/R_{1,\mathrm{h}}$

tion of the optimal compressor design by means of computational fluid dynamics (CFD), and the preliminary structural assessment by means of finite element analysis (FEA).

The paper is structured as follows. First, the methodology is described. Next, the 3D design of the two stages is constructed from the results of the multi-objective conceptual design optimization. Then, the selected design is characterized by means of FEA and CFD. Lastly, concluding remarks summarize the lessons learnt and give a perspective on future work.

METHODOLOGY

Scaling Analysis for Twin-Stage Compressors

The scaling law applied to single-stage centrifugal compressors can be expressed as [7]

$$\boldsymbol{y} = f(\phi_{\mathrm{t1}}, \psi, \alpha_2, \beta, \overline{\gamma_{Pv}}, Re, \boldsymbol{\sigma}). \tag{1}$$

In Eqn. (1), the vector $\boldsymbol{y}$ collects the compressor stage characteristics, e.g., rotational speed, impeller tip radius, and performance metrics, e.g., efficiency, operating range. The vector $\boldsymbol{\sigma}$ groups the non-dimensional geometrical parameters, as listed in Table 1. The stage velocity triangles are univocally defined by the choice of ϕ_{t1}, ψ, and α_2. The work input can be expressed as a function of the compression ratio β. Moreover, the influence of the working fluid and of flow non-ideality can be assessed by computing the average value of the isentropic pressure-volume exponent

$$\gamma_{Pv} = -\frac{v}{P}\frac{\partial P}{\partial v}\bigg|_s = -\frac{v}{P}\frac{c_p}{c_v}\frac{\partial P}{\partial v}\bigg|_T \tag{2}$$

over the prescribed thermodynamic process [8]. Lastly, the impact of viscous effects is determined by evaluating the average value of the Reynolds number throughout the compressor stage.

For a twin-stage compressor, the design process encompasses additional requirements: the mass flow rate and the rotational speed must be equal for the two stages, and the designer has to decide how to split the compression ratio. In order to conceptually address the problem of determining the optimal duty of the two stages, the scaling analysis can be extended as follows. Starting from the definition of the swallowing capacity

$$\phi_{\mathrm{t1}} = \frac{\dot{m}}{\rho_{\mathrm{t1}} U_2 D_2^2} = \frac{2\dot{V}_{\mathrm{t1}}}{D_2^3 \Omega}, \tag{3}$$

and imposing constant rotational speed, the ratio of the flow coefficients of the two stages can be written as

$$\frac{\phi_{\mathrm{t1}}\big|_{\mathrm{s1}}}{\phi_{\mathrm{t1}}\big|_{\mathrm{s2}}} = \frac{D_2^3\big|_{\mathrm{s2}}}{D_2^3\big|_{\mathrm{s1}}} \cdot \frac{\dot{V}_{\mathrm{t1}}\big|_{\mathrm{s1}}}{\dot{V}_{\mathrm{t1}}\big|_{\mathrm{s2}}}. \tag{4}$$

The split of the compression ratio among the two stages can be expressed as a function of the splitting factor κ_{s}

$$\begin{cases} \beta_{\mathrm{tt}}\big|_{\mathrm{s1}} = \kappa_{\mathrm{s}} \sqrt{\beta_{\mathrm{tt}}/\kappa_{\mathrm{s}}} \\ \beta_{\mathrm{tt}}\big|_{\mathrm{s2}} = \sqrt{\beta_{\mathrm{tt}}/\kappa_{\mathrm{s}}} \end{cases} \tag{5}$$

In turn, for a fixed value of mass flow rate in the two stages, assuming constant pressure-volume isentropic exponent over the entire compression process, and neglecting total pressure losses between the outlet of the first impeller and the inlet of the second stage, the ratio of the volumetric flow rates defined at the impeller inlet can be expressed as function of κ_{s}

$$\frac{\dot{V}_{\mathrm{t1}}\big|_{\mathrm{s1}}}{\dot{V}_{\mathrm{t1}}\big|_{\mathrm{s2}}} = \frac{\dot{m}\big|_{\mathrm{s1}}}{\dot{m}\big|_{\mathrm{s2}}} \cdot \frac{\rho_{\mathrm{t1}}\big|_{\mathrm{s2}}}{\rho_{\mathrm{t1}}\big|_{\mathrm{s1}}} = \left(\sqrt{\beta_{\mathrm{tt}} \cdot \kappa_{\mathrm{s}}}\right)^{\frac{1}{\overline{\gamma_{Pv}}}} . \tag{6}$$

Furthermore, rearranging the definition of the work coefficient

$$\psi = \frac{\Delta h_{\mathrm{tt}}}{U_2^2} = \frac{4\Delta h_{\mathrm{tt}}}{\Omega^2 D_2^2} = \frac{4}{\Omega^2 D_2^2} \frac{P_{\mathrm{t1}}}{\rho_{\mathrm{t1}}} \frac{\overline{\gamma_{Pv}}}{\overline{\gamma_{Pv}} - 1} \left. \quad \beta_{\mathrm{tt}}^{\frac{\overline{\gamma_{Pv}}-1}{\overline{\gamma_{Pv}}}} - 1 \right) , \tag{7}$$

it is possible to make explicit the dependence of the ratio of the work coefficients on the splitting factor κ_{s}, and on the ratio between the impeller tip diameters

$$\frac{\psi\big|_{\mathrm{s1}}}{\psi\big|_{\mathrm{s2}}} = \left(\sqrt{\beta_{\mathrm{tt}} \cdot \kappa_{\mathrm{s}}}\right)^{\frac{1}{\overline{\gamma_{Pv}}}-1} \cdot \frac{\left(\sqrt{\beta_{\mathrm{tt}} \cdot \kappa_{\mathrm{s}}}\right)^{\frac{\overline{\gamma_{Pv}}-1}{\overline{\gamma_{Pv}}}} - 1}{\left(\sqrt{\frac{\beta_{\mathrm{tt}}}{\kappa_{\mathrm{s}}}}\right)^{\frac{\overline{\gamma_{Pv}}-1}{\overline{\gamma_{Pv}}}} - 1} \cdot \frac{D_2^2\big|_{\mathrm{s2}}}{D_2^2\big|_{\mathrm{s1}}} . \tag{8}$$

Finally, by combining Eqn. (4), (6), (8), it is possible to relate the flow coefficients ratio with the ratio of the work coefficients, the splitting factor, the overall compression ratio, and the average value of the isentropic exponent over the thermodynamic transformation

$$\frac{\phi_{\mathrm{t1}}\big|_{\mathrm{s1}}}{\phi_{\mathrm{t1}}\big|_{\mathrm{s2}}} = f \left. \quad \frac{\psi\big|_{\mathrm{s1}}}{\psi\big|_{\mathrm{s2}}}, \kappa_{\mathrm{s}}, \beta_{\mathrm{tt}}, \overline{\gamma_{Pv}} \right) . \tag{9}$$

Eqn. (9) is graphically displayed in Fig. 1. By analyzing the trends, one can notice that, with the given design specification, the selection of an equal split of compression ratio among the two stages, i.e., $\kappa_{\mathrm{s}} = 1$, combined with the choice of constant flow coefficient, i.e., $\phi_{\mathrm{t1}}\big|_{\mathrm{s1}} / \phi_{\mathrm{t1}}\big|_{\mathrm{s2}} = 1$, leads to a strong unbalance in the work coefficients, with the second stage facing a higher non-dimensional duty. On the other hand, the higher is the selected ratio of work coefficients, the larger is the resulting flow coefficients ratio. The disparity in the flow coefficients of the two stages is attenuated by increasing the value of κ_{s}, i.e., by increasing the compression ratio of the first stage.

For high-speed miniature centrifugal compressors, the choice of the splitting factor is primarily driven by manufacturing constraints. Given that the second stage inherently features lower volumetric flow rate, its efficiency and operating range are penalized by larger values of relative tip clearance, relative surface roughness, and blade blockage. A viable solution to overcome this limitation consists in selecting $\kappa_{\mathrm{s}} \geq 1$, and maximizing the efficiency of the first stage, i.e., the one responsible for most of the compression ratio. Fig. 2 shows the contours of the total-to-total efficiency and operating range, i.e., $OR = (\dot{m}_{\mathrm{max}} - \dot{m}_{\mathrm{min}})/\dot{m}_{\mathrm{des}}$ at Ω_{des}, of a miniature compressor stage operating with R1233zd(E) [7]. The efficiency of the first stage can be maximized by selecting a design point lying on the locus of optimal ϕ_{t1}, namely the dashed black line. By selecting $\kappa_{\mathrm{s}} \geq 1$, and $\psi\big|_{\mathrm{s1}} / \psi\big|_{\mathrm{s2}} = 1$, and based on (4), the flow coefficient of the second stage results to be on the dashed red line, which also corresponds to the region of optimal operating range. The consequence thereof is that the efficiency of the entire compression process is enhanced, without penalizing the operating range of the twin-stage machine.

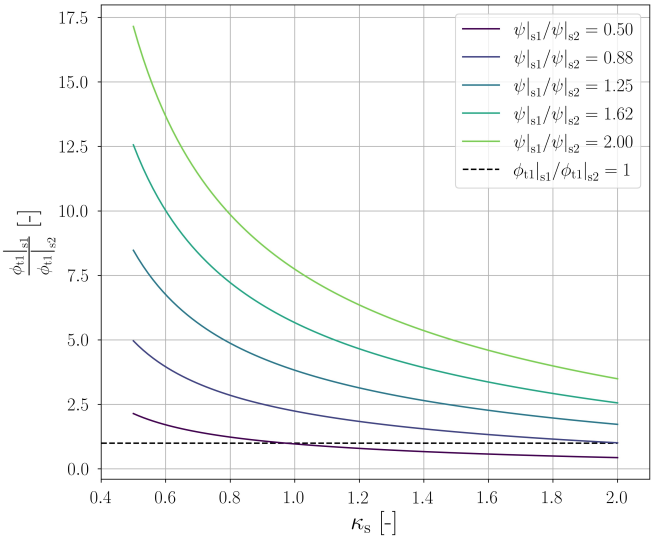

FIGURE 1: Trend of flow coefficients ratio, as function of the splitting factor, and of the work coefficients ratio. The data have been generated considering an overall compression ratio $\beta_{\mathrm{tt}} = 7$, and an average value of isentropic exponent $\overline{\gamma_{Pv}} = 1.075$, corresponding to the design conditions of the IRIS compressor.

Conceptual Design Model

A detailed description of the method used for the conceptual design of single-stage centrifugal compressors can be found in [7]. In this section, only the fundamental building blocks are reviewed, and emphasis is given to the additional procedures needed to cope with the design of twin-stage compressors, as depicted in Fig. 3.

The in-house reduced-order compressor model relies on the lumped parameters approach. However, the flow quantities are evaluated at five different span-wise locations at the inducer sec-

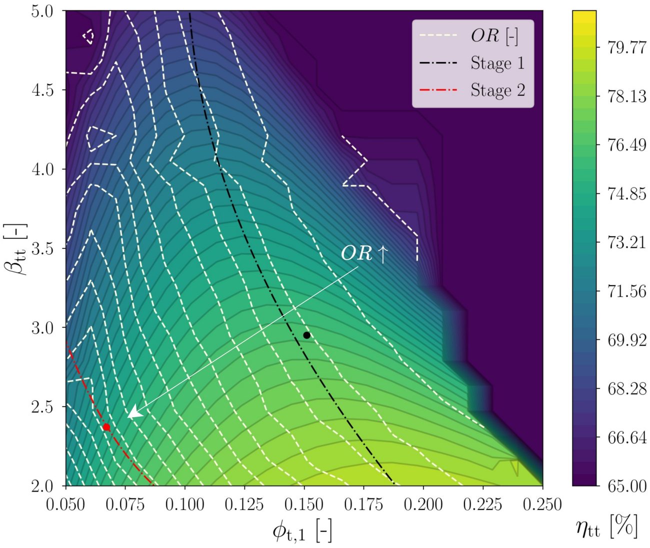

FIGURE 2: Design map of η_{tt} and OR computed for R1233zd(E) at $P_{\mathrm{t1}} = 0.5$ bar, $T_{\mathrm{t1}} = 283.15$, $\psi_{\mathrm{is}} = 0.8$. The dashed black and red lines correspond to the theoretical locii of optimal design for the two stages, computed by maximizing η_{tt} of stage 1 and fixing $\psi|_{\mathrm{s1}}/\psi|_{\mathrm{s2}} = 1$. The black and red dots correspond to the design point selected by the multi-objective optimizer.

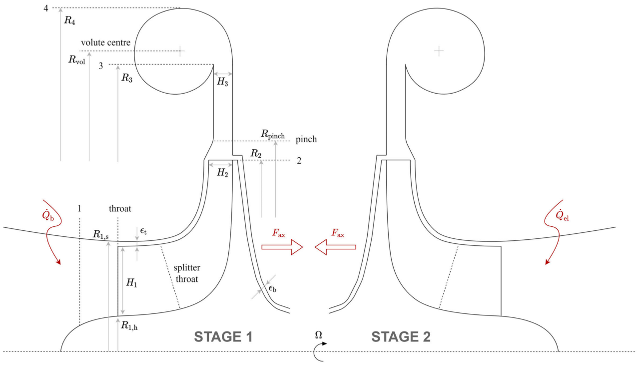

FIGURE 3: Meridional view of a centrifugal compressor, featuring two stages mounted in back-to-back configuration on the same shaft.

tion, to capture the variation of the centrifugal potential over the blade span. The inlet velocity triangle is determined by the choice of the swallowing capacity and by the minimization of the relative Mach number at inducer shroud [11]. The first guess of the outlet velocity triangle is set by the selection of α_2 and of the isentropic work coefficient. The actual work coefficient is then iteratively adjusted to match the target compression ratio, accounting for slip and losses, by means of semi-empirical correlations. The flow in the vaneless diffuser is modelled by integrating the system of two-dimensional differential equations derived by Stanitz [12].

The stage off-design performance is computed according to the following method. First, the choking point at the selected rotational speed is estimated by solving the isentropic mass, momentum, and energy balances between the inlet and throat sections, until the choking conditions are established at each spanwise station. Then, the mass flow rate is progressively reduced and the compressor performance is computed, until either rotating stall conditions are met [13], or the stage efficiency falls below a pre-definied threshold, e.g., $\eta_{\mathrm{tt}} \leq 50\%$. This procedure is repeated over different speed-lines to compute the compressor operating map. In Fig. 4, the predictions of the compressor model are compared with the experimental data of three reference test cases available in literature [5,6,9,10,14,15], and with the CFD simulations of the first stage of the IRIS compressor, whose design is documented in the following. The outcome of the validation study is that more than 95% of the experimental and CFD data fall within the ±5% uncertainty bands of the values predicted by the ROM, except for the data of the EPFL compressor in the close proximity of the choking point, at 210 krpm.

The design of a twin-stage compressor involves additional steps. The two compressor wheels are mounted on the same shaft, thus the rotational speed of the second impeller is constrained by the design of the first stage. In other words, once fixed the design of the first impeller, the choice of the work coefficient of the second stage univocally determines also its flow coefficient, or viceversa. As a consequence, an ad-hoc design strategy is needed to comply with both the requirements of high efficiency and wide operating range, as discussed in the previous section.

In addition to that, the use of gas bearings imposes stringent constraints on the maximum allowable axial thrust generated by the two compressor wheels. To cope with this limitation, it is necessary to adopt a back-to-back configuration and to carefully design the two impellers to balance their axial thrust. In the reduced-order compressor model, this is achieved by estimating the axial thrust of the two stages with the method proposed in [11], and by imposing a constraint on the maximum unbalance, computed over the entire operating range.

Finally, the high compactness requirement for the entire compressor assembly poses additional challenges with regards to bearings and electric motor cooling. In the proposed twin-stage configuration, a small portion of the refrigerant mass flow is bled at the outlet of the first stage and is recirculated at the inlet of the machine, after being used for bearings cooling. On the other hand, the main portion of the pressurized refrigerant vapor leaving the first stage is used to cool the electric motor, before entering the second stage. In this way it is possible to minimize the size, thus the weight, of the compressor assembly, at the expenses of a fluid dynamic efficiency penalty, due to interstage

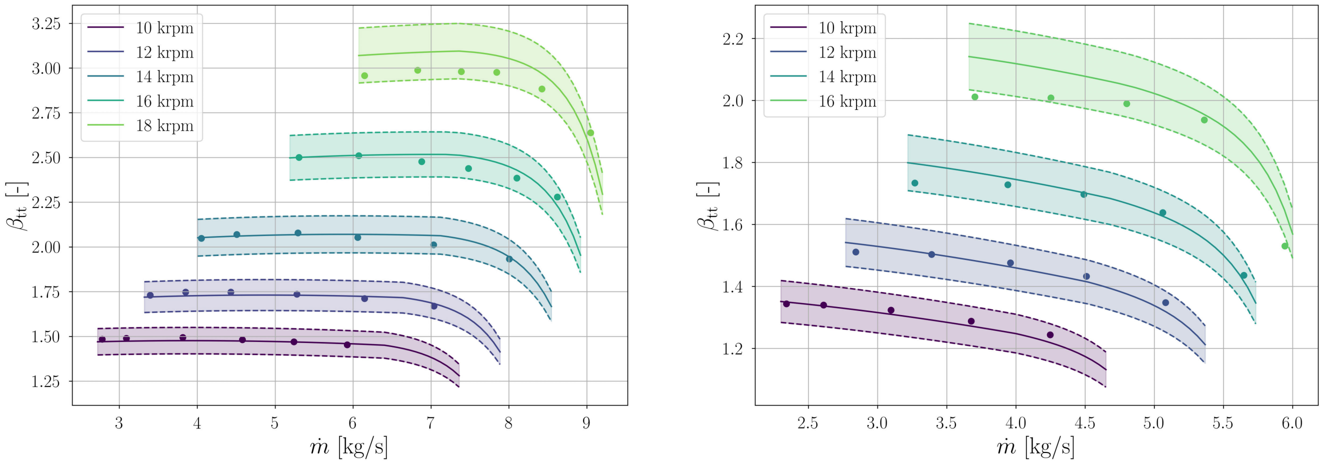

(a) Eckardt O

(b) Eckardt B

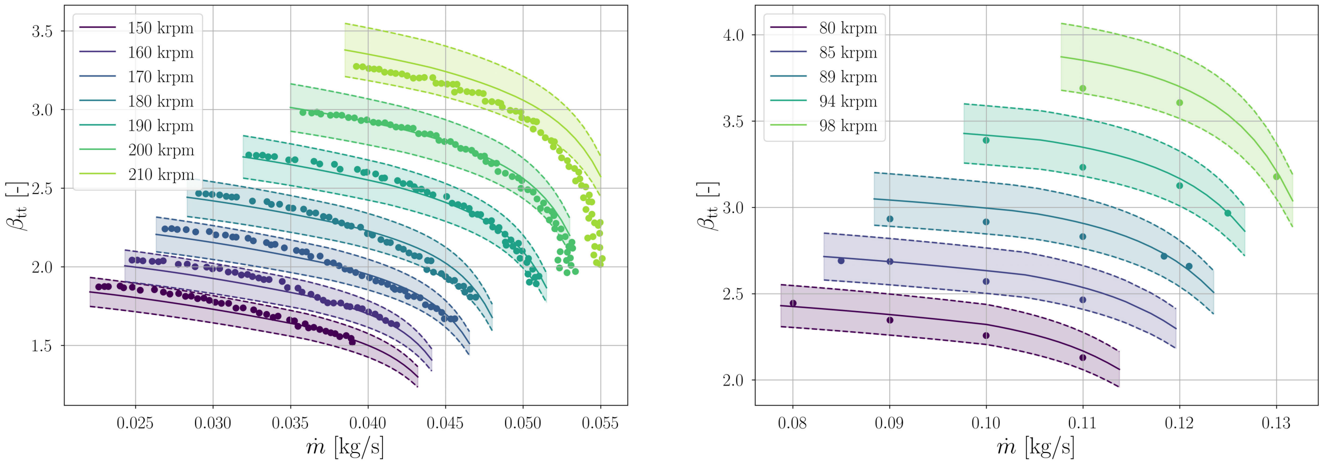

(c) EPFL compressor

(d) IRIS compressor, stage 1

FIGURE 4: Validation of the reduced-order model. Solid lines represent compressor model predictions; dashed lines bound colored $\pm 5\%$ uncertainty bands; dots correspond to experimental data of Eckardt impellers O and B [9, 10], EPFL compressor [6], and CFD simulations of the first stage of the IRIS compressor.

flow heating. A summary of the design procedure implemented in the ROM is presented in Fig. 5.

Multi-Objective Optimization Framework

The twin-stage compressor model has been integrated within a multi-objective optimization framework. The objective functions selected in this work are the operating range, i.e., $OR = (\dot{m}_{\mathrm{max}} - \dot{m}_{\mathrm{min}})/\dot{m}_{\mathrm{des}}$, and the compressor efficiency, both evaluated at the design rotational speed. To account for multiple operating points, the compressor efficiency is computed as the weighted average of the total-to-total efficiency, evaluated over the entire design speed-line. The weights used for this calculation are inversely proportional to the distance of each operating point from the selected design point.

In addition to that, a set of non-linear inequality constraints are imposed to ensure compressor manufacturability. To cope with the choice of the electric motor and the design of the gas bearings, additional inequality constraints are imposed on the rotational speed, the axial thrust, the power, and the torque produced by the two stages. The thresholds defining the maximum allowable axial thrust, power and torque are compared with the

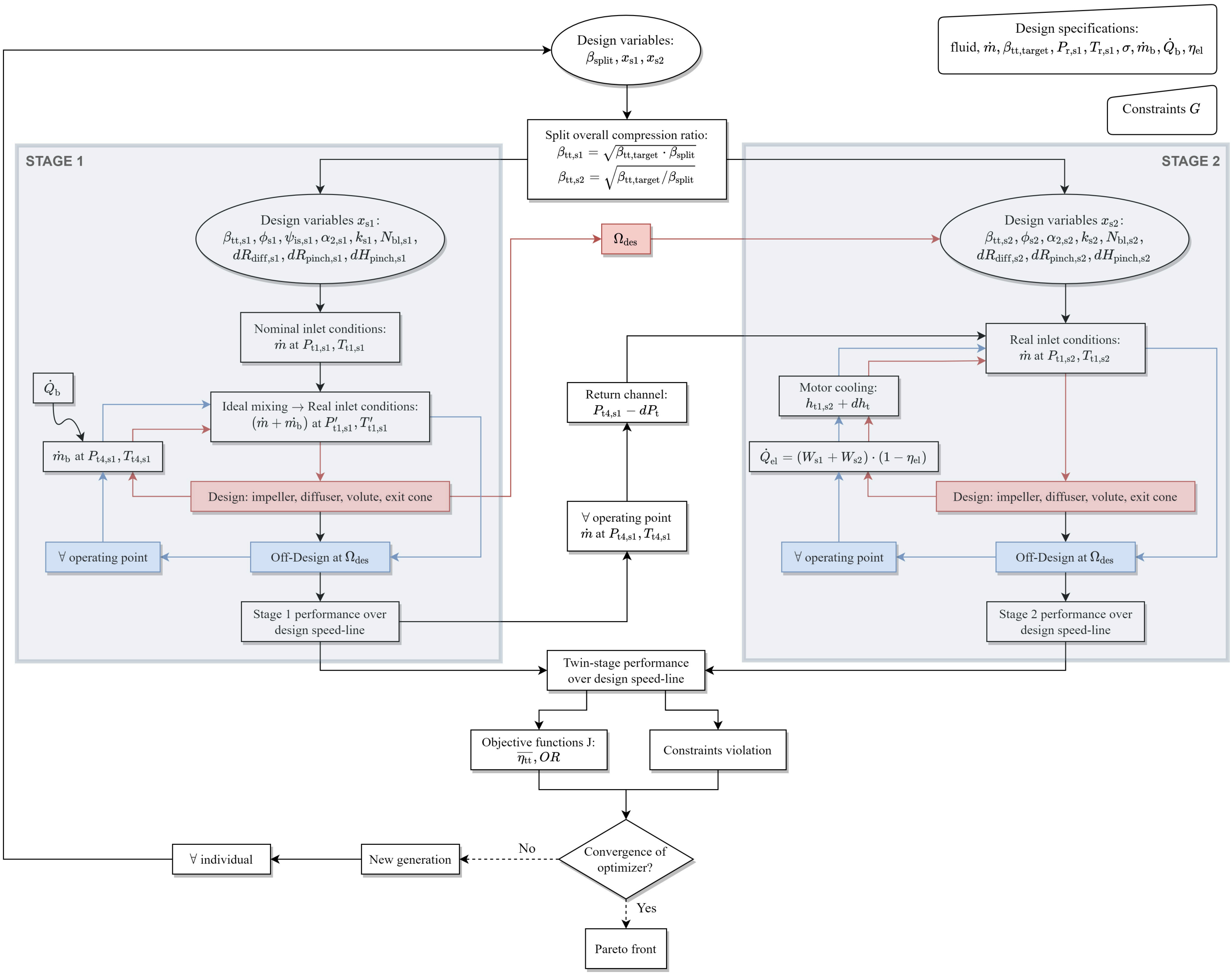

FIGURE 5: Flowchart of the design method implemented in the reduced-order compressor model.

maximum values evaluated over the design speed-line. Overall, the optimization problem comprises 16 design variables, 2 objectives and 16 inequality constraints, as summarized in Table 2.

CASE STUDY

The in-house compressor model coupled to the multi-objective optimization framework has been used to design the twin-stage compressor to be installed in the IRIS facility. The simplified process flow diagram of the test rig is shown in Fig. 6. It consists of a two pressure levels refrigeration cycle resembling the configuration of an ECS for large helicopters, i.e., 19 passengers and 2 pilots. The condenser is an air-to-refrigerant microchannel heat exchanger, operated to reproduce the actual atmospheric conditions of the system, while the evaporator is designed as a water-cooled plate heat exchanger, in order to tightly control the system loading. At a later stage, a second water-cooled evaporator will be integrated in the test rig, to explore the possibility of separately cooling the avionics at a higher temperature.

Conceptual Design

The compressor design specifications, as well as the values set for the constraints, and the bounds selected for the design variables, are listed in Table 2. The values of the additional

TABLE 2: Settings used for the multi-objective optimization of the compressor that will be installed in the IRIS test rig.

Variable	Type	Value
$\beta_{\mathrm{tt,target}}$	Design specification	7
$\dot{m}$	Design specification	0.114 kg/s
fluid	Design specification	R1233zd(E)
$P_{\mathrm{t}1}\|_{\mathrm{s}1}$	Design specification	47.79 kPa
$T_{\mathrm{t}1}\|_{\mathrm{s}1}$	Design specification	283.19 K
$\dot{m}_{\mathrm{b}}$	Design specification	0.0044 kg/s
$\dot{Q}_{\mathrm{b}}$	Design specification	360 W
η_{el}	Design specification	95%
κ_{s}	Optimization variable	0.5-2
$\phi_{\mathrm{t}1}\|_{\mathrm{s}1-\mathrm{s}2}$	Optimization variable	0.06-0.2
$\psi_{\mathrm{is}}\|_{\mathrm{s}1}$	Optimization variable	0.6-1.0
$\alpha_2\|_{\mathrm{s}1-\mathrm{s}2}$	Optimization variable	60°-75°
$k\|_{\mathrm{s}1-\mathrm{s}2}$	Optimization variable	0.65-0.95
$N_{\mathrm{bl}}\|_{\mathrm{s}1-\mathrm{s}2}$	Optimization variable	12-20
$R_3/R_2\|_{\mathrm{s}1-\mathrm{s}2}$	Optimization variable	1.3-2
$R_{\mathrm{r,pinch}}\|_{\mathrm{s}1-\mathrm{s}2}$	Optimization variable	0-1
$H_{\mathrm{r,pinch}}\|_{\mathrm{s}1-\mathrm{s}2}$	Optimization variable	0-1
$\min(R_{1,\mathrm{h}})\|_{\mathrm{s}1-\mathrm{s}2}$	Inequality constraint	3.25 mm
$\min(a)\|_{\mathrm{s}1-\mathrm{s}2}$	Inequality constraint	1 mm
$\min(H_2)\|_{\mathrm{s}1-\mathrm{s}2}$	Inequality constraint	1.35 mm
$\max(R_4)\|_{\mathrm{s}1-\mathrm{s}2}$	Inequality constraint	50 mm
$\max(M_3)\|_{\mathrm{s}1-\mathrm{s}2}$	Inequality constraint	0.6
$\min(\Omega)-\max(\Omega)$	Inequality constraint	50-112 krpm
$\max(\Delta F_{\mathrm{ax}})$	Inequality constraint	26 N
$\max(W_{\mathrm{el}})$	Inequality constraint	6.1 kW
$\max(T)$	Inequality constraint	0.52 Nm

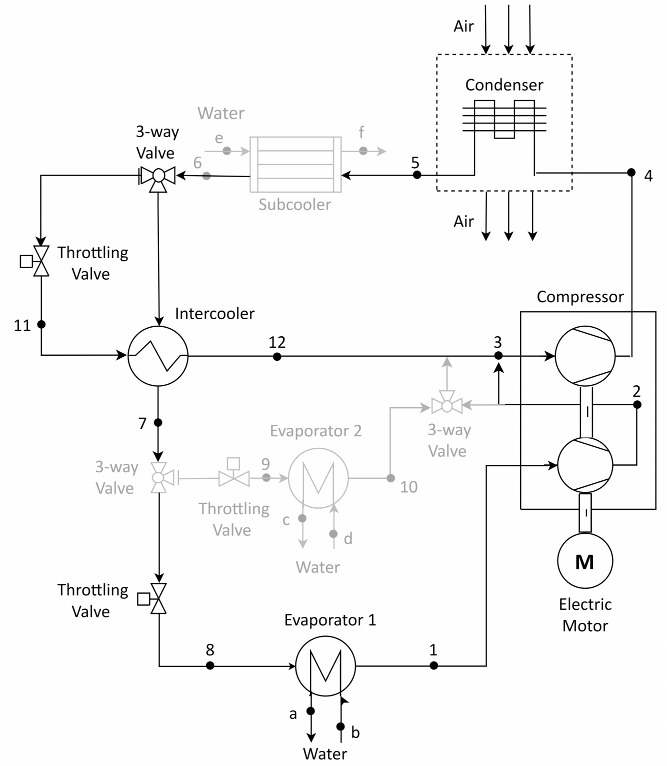

FIGURE 6: Simplified P&ID of the IRIS facility. The shaded components will be integrated in a second phase.

TABLE 3: Geometrical parameters fixed by manufacturing constraints.

Variable	Value	Variable	Value
ε_{b}	0.15 mm	Ra	3.2 µm
$t_{\mathrm{bl,h}}$	0.6 mm	$t_{\mathrm{bl,s}}$	0.3 mm
$\varepsilon_{\mathrm{t,le}}$	0.2 mm	$\varepsilon_{\mathrm{t,te}}$	0.15 mm

geometrical parameters set by manufacturing constraints are reported in Table 3. The Pareto front of the optimal designs is computed by resorting to the NSGA-II algorithm described in [16], and implemented in the open-source library Pymoo [17]. All the optimization variables are floating point, except for the number of blades of the two impellers, which are treated as integers. The initial population comprises ten individuals for each design variable, and is sampled according to the latin hypercube methodology along the floating point directions, and randomly along the integer axes. The population is evolved for 120 generations, leading to a total of 19200 function evaluations.

The optimal conceptual design has been chosen as a trade-off between compressor efficiency and operating range, by giving priority to the second objective, as required by the target application. The values of the design variables corresponding to the

TABLE 4: Design variables corresponding to the compressor design obtained with the multi-objective optimization.

Variable	Stage 1	Stage 2
$\beta_{\text{tt,target}}$	2.95	2.37
ϕ_{t1}	0.151	0.067
$\psi_{\text{is}} - \psi$	0.83-0.66	0.76-0.65
α_2	64.2°	67.4°
k	0.948	0.897
$N_{\text{bl}} - N_{\text{split}}$	7-7	9-9
R_3/R_2	1.521	1.442
R_{pinch}/R_2	1.464	1.383
H_3/H_2	0.717	0.748

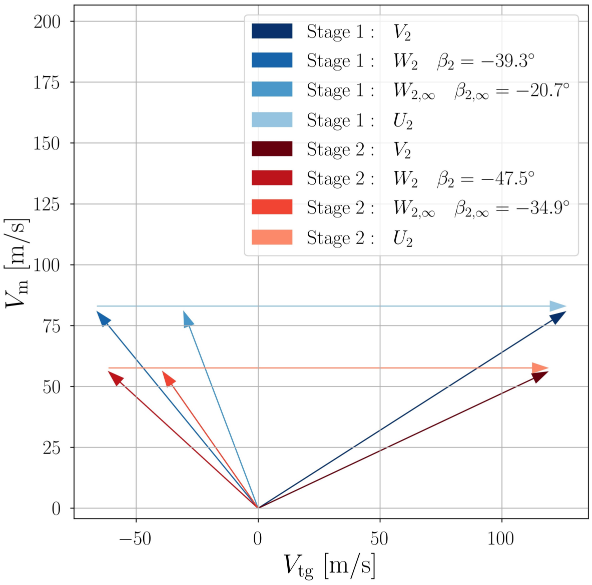

FIGURE 7: Velocity triangles at the impeller outlet of the two optimized compressor stages.

selected design are listed in Table 4. The velocity triangles computed at the outlet of the two optimized impellers are sketched in Fig. 7. With the purpose of showcasing the actual size of the prototype, a 3D printed mock-up of the two optimized impellers is shown in Fig. 8.

By analyzing the results, it is possible to formulate the following considerations. The first impeller is characterized by a higher compression ratio than the second, while the work coefficient is nearly constant for the two stages. Moreover, the first impeller features a value swallowing capacity 2.25 times larger than the one of the second stage. These trends confirm the validity of the design guidelines derived from the extended scaling analysis for twin-stage compressors.

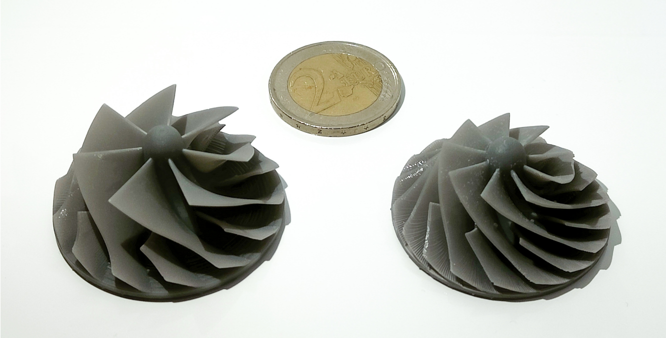

FIGURE 8: 3D printed mock-up of the two impellers designed by means of the multi-objective optimization framework.

Furthermore, one can notice that the second impeller is characterized by a higher backsweep angle, as compared to the first one. The reason of that is inherently related to the small scale of the target application. On one hand, the minimum tip clearance gap is set by manufacturing limitations. On the other hand, the second impeller systematically features a lower blade height, as a result of the lower volumetric flow rate. In turn, the second impeller is always characterized by a higher relative clearance gap, leading to a significant efficiency drop. A viable strategy to limit this decay in efficiency is to decrease the meridional component of the velocity at impeller outlet, such to increase the outlet blade span. This is achieved by designing impeller blades featuring a higher backsweep angle, as depicted in Fig. 7.

Detailed Design

The three-dimensional geometry of the two stages have been constructed from the results of the conceptual design optimization, using a commercial software [18]. The shape of the main and the splitter blades are controlled by specifying the hub, mid, and shroud profiles, and by stacking them along the radial direction at leading edge. To enhance the structural integrity, the wrap angles have been chosen to ensure a rake angle of 18° and 23.5° for the first and second stage, respectively. The meridional location of the splitter blades leading edge have been selected to ensure that the geometrical throat is located in the main blade passage. The blades feature constant thickness distribution in the blade-to-blade plane, and linear tapering in the span-wise direction.

Despite of the described commonalities in the design of the two stages, the impellers exhibit major geometrical discrepan-

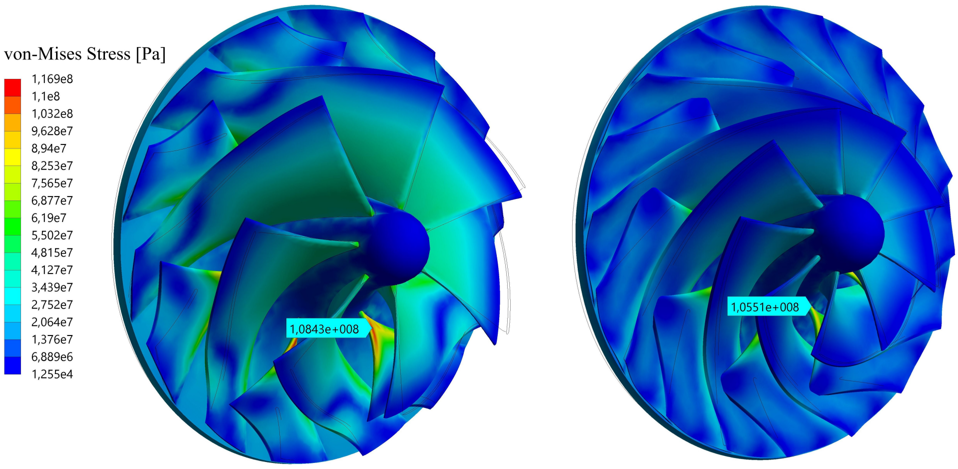

(a) Stage 1 (b) Stage 2

FIGURE 9: Von-Mises stress computed for the two preliminary impeller-shaft assemblies, accounting for the centrifugal load at the maximum rotational speed, i.e., 100 krpm. The deformation of the compressor wheels is amplified by two orders of magnitude, while the wireframes show the shape of the undeformed structures.

TABLE 5: Properties of Al 2219-T852.

Property	Value	Property	Value
ρ	3100 kg/m^3	T_m	913 K
E	72 GPa	ν	0.33
σ_y	360 Mpa	σ_uts	460 Mpa

cies, that can be attributed to the different regime of operation, namely $M_{w1,s}\big|_{\mathrm{s1}} = 1.17$, $M_{w1,s}\big|_{\mathrm{s2}} = 0.77$. Given that the inducer of the first stage is transonic, the blades are designed to be aft-loaded at shroud, to improve the choke margin and reduce the shock losses [19]. Conversely, the blades of the second stage are shaped such to obtain a mid-loaded shroud and an aft-loaded hub, to mitigate the impact of secondary flows, while delaying the formation of the tip leakage vortex in presence of large clearance gap [20, 21]. The vaneless diffuser is characterized by a linear pinch up to 146% and 138% of the outlet impeller radius for stage 1 and stage 2, respectively.

A static structural analysis has been carried out on the preliminary impeller-shaft assemblies to assess their mechanical integrity. Only the centrifugal load at the maximum rotational speed, i.e., 100 krpm, has been considered in the simulations. The properties of the selected material are listed in Table 5. As shown in Fig. 9, the maximum von-Mises stress is located at the leading edge of the splitter blades for the two impellers, whereas the blades trailing edge are relatively unloaded, due to the beneficial effect of the adopted rake angles. The maximum stresses computed for stage 1 and stage 2 are approximately 108 Mpa, and 106 Mpa, leading to a safety factor of about 3.36 with the respect to the yielding stress of the selected material. The combined effect of the centrifugal and the aerodynamic loads will be investigated in the following design iteration, together with the characterization of the dynamic response of the system.

CFD ANALYSIS

Hybrid Computational Method

The fluid dynamic performance of the compressor prototype has been characterized by resorting to a hybrid framework that encompasses CFD models and ROMs, as schematically described in Fig. 10. The flow field throughout the impeller and the diffuser of the two stages is computed with CFD. The influence of the remaining components along the main flow path, i.e., volute, exit cone, and return channel, is accounted for by means of ROMs. The choice of this modeling approach is motivated as follows. First, the prescribed compressor configuration, featuring two impellers mounted back-to-back on the same shaft, implies the presence of a volute at the outlet of each stage. Consequently, the use of a single CFD model to compute the flow field throughout the entire machine would require full annulus simulations. In turn, this leads to a sizeable computational overhead, and ultimately hinders the simulation of multiple compressor operating points. Moreover, in contrast to other turbomachinery configurations, in a twin-stage compressor the flow field at the inlet of the second stage is only weakly coupled to the one at the out-

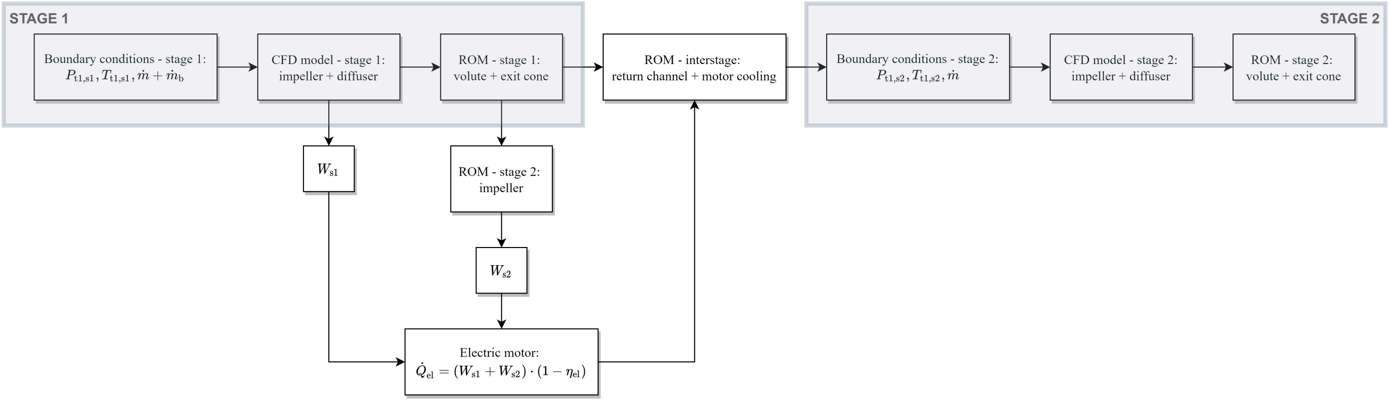

FIGURE 10: Flowchart of the hybrid computational method used to reproduce the operating map of the IRIS compressor.

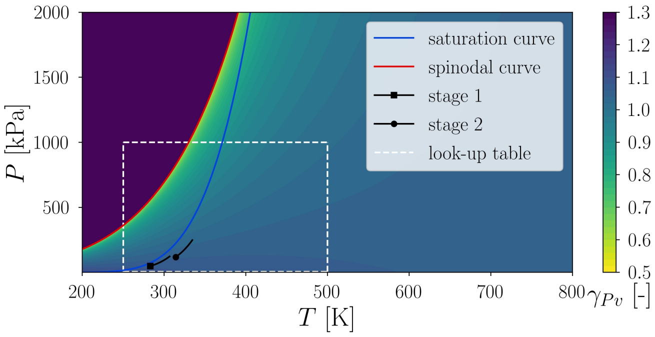

FIGURE 11: Look-up table used to speed-up the evaluation of the thermo-physical fluid properties. The vapor properties are extended up to the spinodal line, to improve solver robustness in the initial phase of the calculation.

let of the adjacent blade row, i.e., the impeller of the first stage. Hence, the benefits deriving from the use of a single CFD model for the entire compressor are not deemed as sufficient to justify the considerable increase of computational cost.

Single passage RANS computations [22] with a frozen-rotor interface are used to assess the fluid dynamic performance of the impeller and the diffuser of the two stages. The boundary conditions are imposed in terms of flow direction, total pressure, and total temperature at the inlet, whereas the mass flow rate is assigned at the outlet. The flow direction is assumed to be normal at the inlet of the two stages. The $k-\omega$ SST turbulence model is employed, together with adequate cell clustering near the walls to guarantee $y+ \leq 1$. Turbulence boundary conditions are set in terms of inlet turbulence intensity ($k = 5\%$), and eddy viscosity ratio ($\mu/\mu_t = 10$), while the turbulent Prandtl number is set to $Pr_t = 1$, in accordance with what documented in [23]. The advective and turbulent fluxes are discretized with a total variation diminishing scheme [24]. A look-up table method is employed to speed-up the evaluation of the thermo-physical fluid properties. The property values are calculated using the multiparameter equation of state model available in [25]. Fig. 11 shows the tabulated region, together with the saturation curve, the spinodal line, and the target isentropic compression processes in the $P-T$ thermodynamic plane. The vapor properties are extended up to the spinodal line to improve solver robustness in the initial phase of the calculation, without affecting the accuracy of the converged solution. After performing a sensitivity analysis on the first compressor stage simulated at design point, see Fig. 12, a grid size of approximately 3.7 million cells, and a thermodynamic mesh of 1 million elements are set as optimal trade-off between accuracy and computational cost. The computational grid of the second stage has been scaled, accounting for the variation of the average Reynolds number, and of the number of blade passages, leading to a grid size of approximately 3.3 million nodes.

The mass-flow averaged flow properties computed by CFD at the outlet of the first diffuser are passed to the ROMs of the volute, exit cone, and return channel, leading to a first estimate of $P_{t1}\big|_{s2}$ and $T_{t1}\big|_{s2}$, in absence of electric motor cooling. Then, the power required by the second impeller is estimated with a ROM, and it is used to compute the overall power input of the electric motor, at the prescribed operating point. Next, the total thermodynamic state at the inlet of the second stage is re-computed, by accounting for electric motor cooling, assuming a constant $\eta_{el} = 95\%$. Finally, the flow conditions at the outlet of the second stage are computed by resorting to the coupling between the CFD models of the impeller and the diffuser, and the ROMs of the volute and the exit cone.

Results

The performance of the compressor prototype has been characterized by means of a total of 54 CFD simulations, ranging from 90% to 110% of the design rotational speed, i.e., 89.7

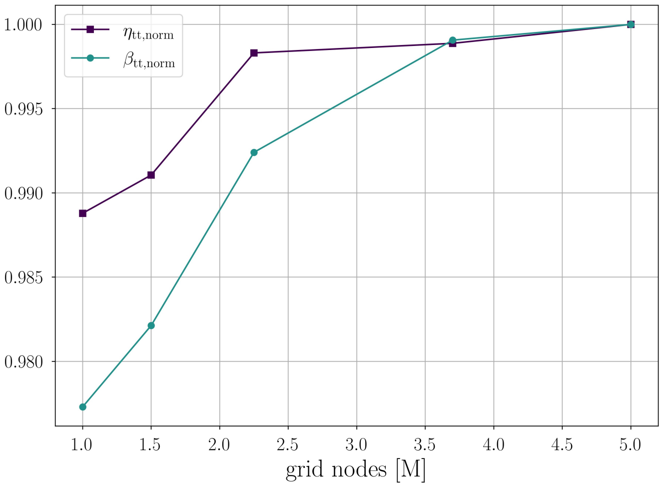

(a) Stage performance metrics

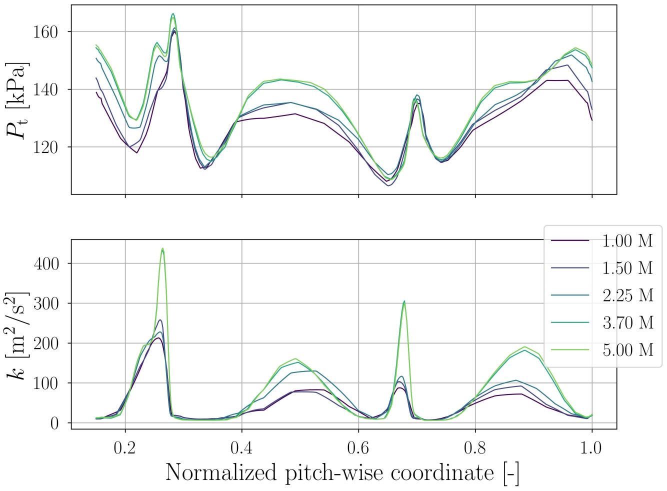

(b) Pitch-wise distribution of total pressure and turbulence kinetic energy at the outlet of the impeller

FIGURE 12: Grid sensitivity analysis performed on stage 1 at design point.

krpm. The left and right boundaries of each speed-line are defined by the numerical prediction of the onset of unsteady flow phenomena, and by the establishment of choking conditions, respectively. To get a more accurate estimation of the inception of rotating stall, it is necessary to resort to higher order calculations, e.g., full annulus URANS. However, this is beyond the scope of the present work. The resulting stable operating points are displayed in Fig. 13, along with the corresponding η_{tt} predictions. The efficiency values are referred to the entire compressor, including the influence of motor cooling, which accounts for $\Delta\eta_{\text{tt}} \approx 4\%$. One can notice that, despite the detrimental effects of motor cooling and small size, it is possible to achieve an average efficiency higher than 70%, with a maximum compression ratio exceeding 9, and an operating range of 0.27 at the design rotational speed.

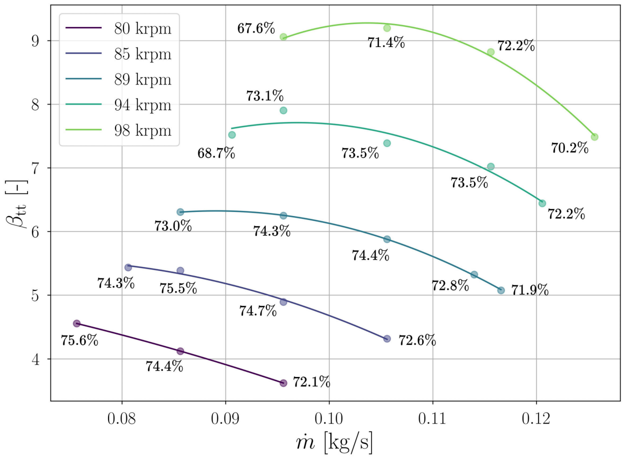

FIGURE 13: Operating map of the IRIS compressor, computed with the method schematically displayed in Fig. 10. The results are reported in terms of mass-flow averaged β_{tt} and η_{tt}.

To evaluate the influence of the tip clearance gap on the performance of such miniature impellers, the CFD simulations of the first stage at the design speed-line have been performed by prescribing $\varepsilon_{\text{t,le}} = 0.4-0.2-0.0$ mm, and $\varepsilon_{\text{t,te}} = 0.3-0.15-0.0$ mm, respectively. The flow field observed downstream of the impeller at design point is displayed in Fig. 15, in terms of total pressure and relative flow angle. In absence of tip clearance gap, the impeller outflow angle is nearly constant over the blade span, with the exception of the shroud region, where flow separation takes place. The leakage flow has a negligible effect on this trend, up to approximately 80% of the blade channel height, where backflow starts to occur. This effect is nearly invariant with respect to the size of the tip clearance gap. Moreover, in absence of tip gap, the total pressure shows a flat profile away from the boundary layers, with some fluctuations induced by flow separation. Conversely, the effect of tip clearance is such that the total pressure exhibits a decreasing trend from midspan to shroud. This phenomenon is more prominent in presence of a larger clearance gap. Similar trends are observed over the entire speed-line. The result thereof is that, when designing a miniature impeller featuring a relative tip gap ε_t/H_2 exceeding 5%, one should account for a reduction of β_{tt}, that is proportional to the relative clearance gap and the compression ratio itself. Such empirical approach has been employed to tune the compressor ROM, and to obtain the results displayed in Fig. 4d.

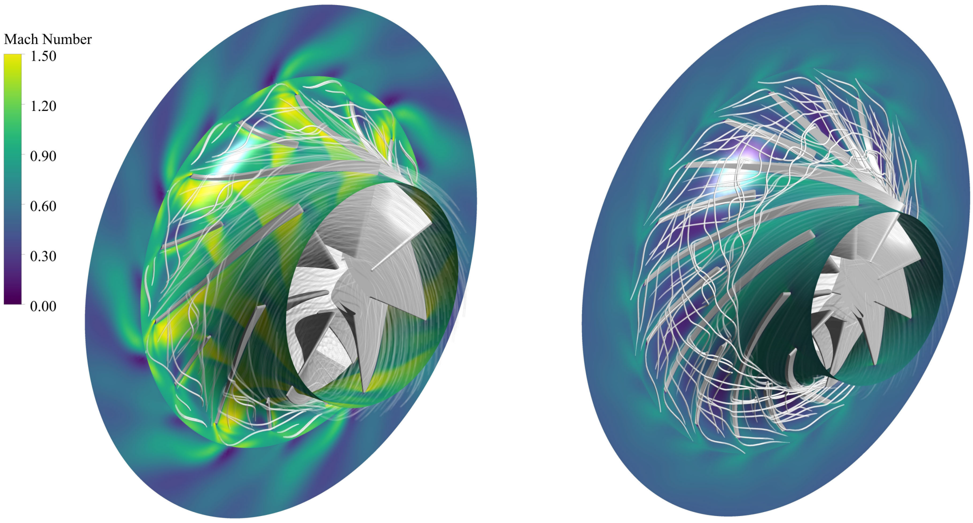

(a) Stage 1

(b) Stage 2

FIGURE 14: Flow field computed by CFD at design point. The Mach number contours are shown at 80 % of the blade channel height. 3D streamlines are colored according to the local value of entropy, to highlight the tip leakage vortex.

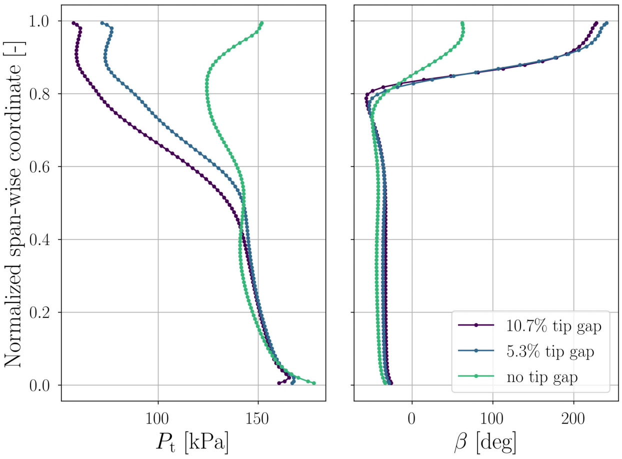

FIGURE 15: Span-wise distribution of total pressure and relative flow angle at the outlet of the first impeller, computed by 3D RANS in presence of variable tip clearance gap. The displayed quantities are mass-flow averaged over the pitch-wise direction.

CONCLUSIONS

The multi-objective design of the high-speed twin-stage compressor, to be installed in the IRIS test rig at Delft University of Technology, has been carried out. The scaling analysis for single-stage centrifugal compressors has been extended to address the optimal design of twin-stage machines. The conceptual design has been performed by means of an in-house ROM, coupled to a multi-objective optimization framework. The fluid dynamic performance and the structural integrity of the optimal design have been assessed by means of a hybrid framework coupling 3D RANS and ROMs, and by FEA. The outcomes of this study can be summarized as follows.

1. When dealing with the design of miniature twin-stage compressors, the efficiency and the operating range of the second stage are inherently penalized by lower values of volumetric flow rate, thus by larger values of relative tip clearance, relative surface roughness, and blade blockage. As a result, the optimal set of non-dimensional parameters is such that the first stage features a larger compression ratio, and a value of swallowing capacity in the proximity of the locus of optimal efficiency. In turn, by selecting the same value of work coefficient for the two stages, the flow coefficient of the second impeller lies in the region of optimal operating range. Consequently, the efficiency of the entire compression process is enhanced, without penalizing the operating range of the twin-stage machine.
2. The results of the multi-objective optimization corroborate the outcomes of the extended scaling analysis. This finding confirms both the suitability of the proposed methodology for the conceptual design optimization of twin-stage compressors, and the validity of the design guidelines derived from similarity principles.
3. It is possible to design a twin-stage compressor for the target application featuring an average efficiency higher than 70%,

a maximum compression ratio exceeding 9, and an operating range of 0.27 at the design rotational speed, despite the detrimental effects of motor cooling and miniature size.

4. The presence of a large tip clearance gap leads to a reduction of β_{tt}, that must be accounted for at preliminary design, in order to achieve the target compression ratio. For the given design of the first stage, a relative tip gap of 5.3% and 10.7% leads to an average reduction of total pressure at impeller outlet of 11.0% and 16.8%, respectively, as computed by CFD over the design speed-line.

ACKNOWLEDGMENT

This research was supported by the Dutch Technology Foundation TTW, Applied Science Division of NWO, the Technology Program of the Ministry of Economic Affairs, and by Aeronamic BV (Grant No. 17091).

REFERENCES

[1] Rutherford, D., Zeinali, M., Arrowsmith, S., Rindlisbacher, T., Eyers, C., Peeters, P., Simos, D., Johnson, T., and Dings Our, J., 2009. "Efficiency Trends for New Commercial Jet Aircraft 1960–2008".

[2] Pollok, A., Bonarini, A., and Casella, F., 2018. "Modelling and control of aircraft environmental control systems". PhD thesis, Politecnico di Milano.

[3] Bender, D., 2018. "Exergy-based analysis of aircraft environmental control systems and its integration into model-based design". PhD thesis, Technische Universität Berlin.

[4] Boeing, 2007. "AERO magazine, 4th quarter".

[5] Schiffmann, J., and Favrat, D., 2009. "Experimental investigation of a direct driven radial compressor for domestic heat pumps". *International Journal of Refrigeration,* ***32***(8), dec, pp. 1918–1928.

[6] Schiffmann, J., and Favrat, D., 2010. "Design, experimental investigation and multi-objective optimization of a small-scale radial compressor for heat pump applications". *Energy,* ***35***(1), jan, pp. 436–450.

[7] Giuffre', A., Colonna, P., and Pini, M., 2022. "The Effect of Size and Working Fluid on the Multi-Objective Design of High-Speed Centrifugal Compressors". *submitted to International Journal of Refrigeration.*

[8] Giuffre', A., and Pini, M., 2021. "Design Guidelines for Axial Turbines Operating With Non-Ideal Compressible Flows". *Journal of Engineering for Gas Turbines and Power,* ***143***(1), jan.

[9] Eckardt, D., 1977. Doctoral Dissertation. Tech. rep.

[10] Japikse, D., 1987. "A critical evaluation of three centrifugal compressors with pedigree data sets: Part 5-studies in component performance". *Journal of Turbomachinery,* ***109***(1), jan, pp. 1–9.

[11] Rusch, D., and Casey, M., 2013. "The design space boundaries for high flow capacity centrifugal compressors". *Journal of Turbomachinery,* ***135***(3), mar.

[12] Stanitz, J., 1952. One-dimensional compressible flow in vaneless diffusers of radial-and mixed-flow centrifugal compressors, including effects of friction, heat transfer and area change. Tech. rep.

[13] Kobayashi, H., Nishida, H., Takagi, T., Fukushima, Y., Kobayashi, H., Nishida, H., Takagi, T., and Fukushima, Y., 1990. "A study on the rotating stall of centrifugal compressors. II - Effect of vaneless diffuser inlet shape on rotating stall". *JSMET,* ***56***, pp. 2646–2651.

[14] Eckardt, D., 1975. "Instantaneous measurements in the jet-wake discharge flow of a centrifugal compressor impeller". *Journal of Engineering for Gas Turbines and Power,* ***97***(3), jul, pp. 337–345.

[15] Eckardt, D., 1976. "Detailed flow investigations within a high-speed centrifugal compressor impeller". *Journal of Fluids Engineering, Transactions of the ASME,* ***98***(3), sep, pp. 390–399.

[16] Deb, K., Pratap, A., Agarwal, S., and Meyarivan, T., 2002. "A fast and elitist multiobjective genetic algorithm: NSGA-II". *IEEE Transactions on Evolutionary Computation,* ***6***(2), apr, pp. 182–197.

[17] Blank, J., and Deb, K., 2020. "Pymoo: Multi-Objective Optimization in Python". *IEEE Access,* ***8***, pp. 89497–89509.

[18] ANSYS Inc., 2019. ANSYS Academic Research BladeGen, Release 19.3.

[19] Casey, M., and Robinson, C., 2021. *Radial Flow Turbocompressors: Design, Analysis, and Applications*, 1st ed. Cambridge University Press.

[20] Zangeneh, M., Goto, A., and Harada, H., 1998. "On the Design Criteria for Suppression of Secondary Flows in Centrifugal and Mixed Flow Impellers". *Journal of Turbomachinery,* ***120***(4), oct, pp. 723–735.

[21] Javed, A., Arpagaus, C., Bertsch, S., and Schiffmann, J., 2016. "Turbocompresseurs de petite taille pour un fonctionnement sur une large plage avec des jeux radiaux importants pour un concept de pompe à chaleur bi-étagée". *International Journal of Refrigeration,* ***69***, sep, pp. 285–302.

[22] ANSYS Inc., 2019. ANSYS Academic Research CFX, Release 19.3.

[23] Otero R., G. J., Patel, A., Diez S., R., and Pecnik, R., 2018. "Turbulence modelling for flows with strong variations in thermo-physical properties". *International Journal of Heat and Fluid Flow,* ***73***, oct, pp. 114–123.

[24] Barth, T., and Jespersen, D., 1989. "The design and application of upwind schemes on unstructured meshes".

[25] Lemmon, E. W., Bell, I. H., Huber, M. L., and McLinden, M. O., 2018. NIST Standard Reference Database 23: Reference Fluid Thermodynamic and Transport Properties-REFPROP, Version 10.0, National Institute of Standards and Technology.